

Determining the ${}^9\text{Be}(n, \gamma){}^{10}\text{Be}$ integral cross section at fission neutron energies

J. J. Goodell^{1,*}, J. A. Church,¹ C. C. Keith,² N. K. Harward,¹ B. Pierson,³ S. Tumey,¹ C. Dorais,¹ and B. B. Bandong¹

¹Lawrence Livermore National Laboratory, 7000 East Avenue, Livermore, California 94550, USA

²Los Alamos National Laboratory, P.O. Box 1663, Los Alamos, New Mexico 87545, USA

³Pacific Northwest National Laboratory, 902 Battelle Boulevard, Richland, Washington 99352, USA



(Received 14 August 2023; accepted 8 December 2023; published 31 January 2024)

Background: The ${}^9\text{Be}$ neutron capture cross section has significant implications for Be materials in the nuclear industry as well as the α process in stellar nucleosynthesis. While the cross section is well constrained at thermal neutron energies, there is a lack of experimental data at higher neutron energies, and the evaluated nuclear data libraries can differ by up to two orders of magnitude.

Purpose: We calculate the ${}^9\text{Be}(n, \gamma){}^{10}\text{Be}$ integral cross section at fission neutron energies in an effort to resolve disagreements amongst the nuclear data libraries.

Methods: Foil irradiation experiments were performed using the Flattop critical assembly at the National Criticality Experiments Research Center with either the highly enriched U or Pu cores, with target foil stacks placed at multiple locations to exploit different neutron energy profiles. Accelerator mass spectrometry was used to measure the ${}^{10}\text{Be}/{}^9\text{Be}$ ratio in irradiated Be foils, while all other activation products were quantified through gamma spectrometry. The experiments were simulated using the Monte Carlo N -Particle radiation transport code and combined with experimental results to determine the total neutron fluence, while the STAYSL-PNNL suite and FISPACT-II code were used to validate the model and assess the systematic uncertainty.

Results: The new ${}^9\text{Be}(n, \gamma){}^{10}\text{Be}$ integral cross sections calculated in this work are $26.5 \pm 2.2 \mu\text{b}$ at 0.59 ± 0.07 MeV, $24 \pm 3 \mu\text{b}$ at 0.98 ± 0.14 MeV, $21.7 \pm 1.3 \mu\text{b}$ at 1.26 ± 0.11 MeV, $21.8 \pm 1.4 \mu\text{b}$ at 1.32 ± 0.11 MeV, and $18.6 \pm 1.1 \mu\text{b}$ at 1.46 ± 0.13 MeV. These results do not agree with integral cross sections from any of the nuclear data library evaluations.

Conclusions: Discrepancies between the new integral cross sections reported here and the nuclear data libraries suggest a more complex cross-section structure in the MeV range which allows for more resonance contributions, and more work is needed to further constrain the evaluated cross sections.

DOI: [10.1103/PhysRevC.109.014625](https://doi.org/10.1103/PhysRevC.109.014625)

I. INTRODUCTION

The neutron activation of Be plays an important role in many applications in the nuclear industry as well as stellar nucleosynthesis in astrophysics. A recent review by Wroblewska *et al.* [1] discusses the issues surrounding safety and operations in material test reactors regarding neutron activations generating reactor poison buildup and degradation of Be components. In stellar nucleosynthesis, the neutron capture reaction on ${}^9\text{Be}$ is an important reaction channel for determining ${}^{12}\text{C}$ formation rates leading to the α process [2–4]. The neutron capture reaction on ${}^9\text{Be}$ is of particular interest in these applications because of the lack of experimental data and discrepancies among the major evaluated nuclear data libraries. This issue is shown in Fig. 1, where there is agreement of the ${}^9\text{Be}(n, \gamma){}^{10}\text{Be}$ cross section at thermal neutron energies, but differences of up to two orders of magnitude in the few-MeV range. These differences at higher energies could have significant implications depending on the application, so it is of interest to the nuclear data community to work to add

additional experimental data in the MeV range and improve agreement between the nuclear data libraries.

Thus far, the experimental work [5–9] has focused solely on thermal neutron energies (see Fig. 1), the exception being a recent paper by Wallner *et al.* [5] providing cross-section values of $8.4 \pm 1.0 \mu\text{b}$ at 0.473 ± 0.053 MeV and $10.6 \pm 0.6 \mu\text{b}$ for a Maxwell-Boltzmann neutron spectrum with $kT = 0.025$ MeV. The consequence is that the evaluated nuclear data libraries are anchored together at lower neutron energies but diverge once neutron energies reach 100 eV. As neutron energies increase beyond 100 eV, the cross section is dependent on the evaluator and theoretical models that have yet to be constrained by experimental data. There are significant differences between the libraries at fission neutron energies that need to be addressed.

As shown in Fig. 1, the libraries exhibit a $1/\nu$ dependence, up to 100 eV. From there, JENDL-4.0u [10] continues as $1/\nu$, while ENDF-B/VIII.0 [11] and TENDL-2019 [12] (based on ENDF-B/VIII.0), have a slight modification due to the consideration of additional data in the evaluation. The CENDL-3.2 [13] library breaks from $1/\nu$ at 100 eV and then holds constant at $100 \mu\text{b}$ from 1 keV up to 20 MeV. The BROND-3.1 [14], equivalent to JEFF-3.3 [15], and EAF-2010

*goodell3@llnl.gov

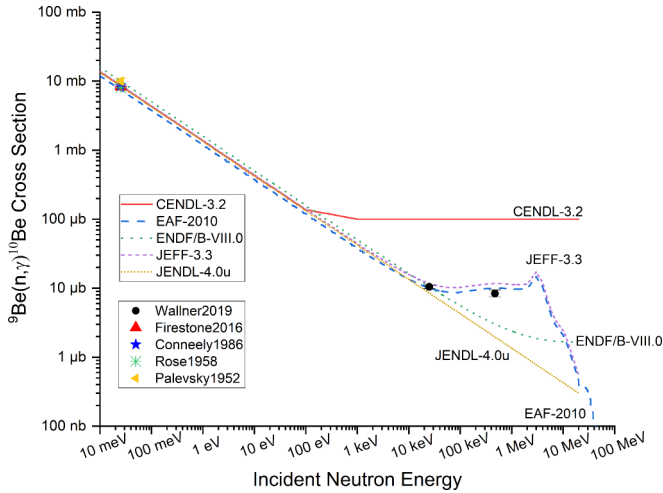


FIG. 1. Plot of ${}^9\text{Be}(n, \gamma){}^{10}\text{Be}$ cross sections from the major libraries and existing experimental data [5–16]. The BROND-3.1 library, equivalent to JEFF-3.3, and the TENDL-2019 library, equivalent to ENDF/B-VIII.0, have been omitted for clarity.

[16] libraries all use a similar treatment traced back to the EAF-2001 evaluation [17], which includes considerations for individual resonances and the direct radiative capture model, differing in choice of thermal cross-section value. Additional analyses by Wallner *et al.* [5] and Mohr [18] also provide evidence supporting a more complex cross section with emphasis on resonances in the direct capture model at 622 and 811 keV. It is also useful to note here that Mughabghab [19] identifies additional unresolved resonances at 2.710 and 2.850 MeV.

This work provides additional data for the ${}^9\text{Be}(n, \gamma){}^{10}\text{Be}$ reaction by determining the integral cross section at fission neutron energies through foil irradiation experiments using the Flattop critical assembly [20] at the National Criticality Experiments Research Center (NCERC) of the Nevada

National Security Site. A series of target foils were placed at different positions within the critical assembly, providing different neutron environments during the same experiment. Two separate experiments were performed: one using the highly enriched uranium (FT-HEU, 93% ${}^{235}\text{U}$) core [21] and the other using the Pu (FT-Pu, 4.8% ${}^{240}\text{Pu}$) core. The experiments were combined with simulations to determine the total neutron fluence for each run and to assess the uncertainty of the method.

II. METHODOLOGY

Integral cross sections of the ${}^9\text{Be}(n, \gamma){}^{10}\text{Be}$ reaction were determined by combining experimental results with simulation. A block diagram of the methodology is presented in Fig. 2, describing the coupling of experimental and simulation components. The foil activation experiments were performed using NCERC’s Flattop critical assembly with separate experiments using the HEU and Pu cores (details of the assembly are provided in Ref. [20]). The ${}^{10}\text{Be}/{}^9\text{Be}$ ratio in activated Be metal foils was measured through accelerator mass spectrometry (AMS) while all other activation products were quantified using gamma spectrometry (a detailed analysis of the activation products is reported in [21]). A simulation of each experimental setup was performed using the Monte Carlo *N*-Particle (MCNP) radiation transport code version 6.3 [22] to estimate the neutron energy profile at each foil pack location and to account for neutron spectrum differences due to the different cores. Simulated neutron distributions were coupled with experimental results from the assay of Au flux monitor foils to estimate the neutron flux at each location. The STAYSL-PNNL suite [23] was used to perform spectral adjustments based on experimental reaction rates, while the FISPACT-II [24] code was used as a secondary check to validate the method and assess the systematic uncertainty of the model. Total neutron fluence values and systematic uncertainties from

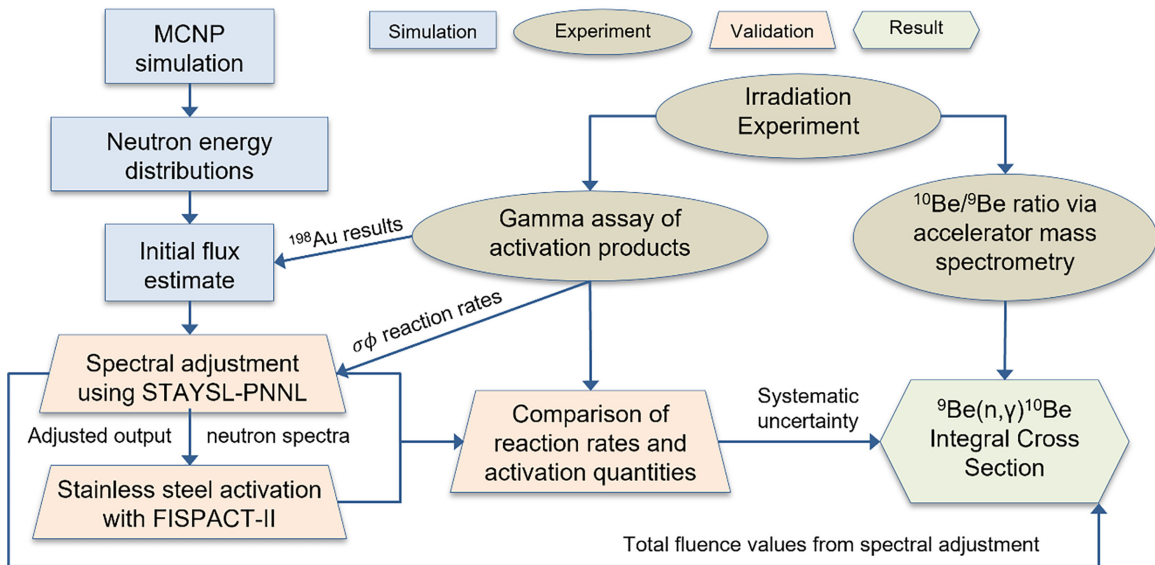


FIG. 2. Block diagram of the methodology coupling experiment and simulation to calculate the integral cross section for the ${}^9\text{Be}(n, \gamma){}^{10}\text{Be}$ reaction. Blue rectangle–simulation; Tan oval–experiment; Orange trapezoid–validation; Green hexagon–result.

the validation process were combined with AMS results to calculate the integral cross section and final uncertainties.

The approach begins with recognizing that the ${}^{10}\text{Be}$ activation product is a pure beta emitter with an extremely long half-life, $(1.387 \pm 0.012) \times 10^6$ yr [25–26], making a radiation-based measurement approach unfitting for this analysis. Instead, the ${}^{10}\text{Be}/{}^9\text{Be}$ ratio was measured at the Lawrence Livermore National Laboratory Center for Accelerator Mass Spectrometry [27]. The AMS method has proven to be useful for ultra-trace-level isotope ratio measurements for a variety of long-lived radionuclides, including ${}^{10}\text{Be}$, ${}^{14}\text{C}$, ${}^{53}\text{Mn}$, ${}^{63}\text{Ni}$, ${}^{93}\text{Zr}$, several actinide isotopes, and others due to the selectivity, sensitivity, and precision of the method [5,28–37].

The production rate of ${}^{10}\text{Be}$ is described by the general rate equation

$$dN_p/dt = n_0\Phi\bar{\sigma} - \lambda_p N_p, \quad (1)$$

where N_p is the number of ${}^{10}\text{Be}$ product nuclei, λ_p is the decay constant for ${}^{10}\text{Be}$, n_0 is the number of ${}^9\text{Be}$ target atoms, Φ is the total neutron flux, and $\bar{\sigma}$ is the 1-group flux-weighted reaction cross section defined by the energy dependent neutron flux probability $P_n(E_i)$ and energy dependent cross section $\sigma(E_i)$ according to

$$\bar{\sigma} = \sum_i P_n(E_i) \sigma(E_i). \quad (2)$$

Since ${}^{10}\text{Be}$ is a long-lived nuclide and effectively stable in the timescale of these experiments, the decay term $\lambda_p N_p$ of Eq. (1) can be neglected, making the calculation independent of half-life. The result is Eq. (3), where for a given ${}^9\text{Be}$ target (n_0) the amount of ${}^{10}\text{Be}$ produced only depends on the number of neutrons on target and the one-group reaction cross section:

$${}^{10}\text{Be} = {}^9\text{Be} \Phi_{\text{total}} \bar{\sigma}. \quad (3)$$

Therefore, only the total neutron fluence Φ_{total} and the ${}^{10}\text{Be}/{}^9\text{Be}$ ratio are needed to calculate the experimental integral cross section $\bar{\sigma}_{\text{exp}}$, by rearranging Eq. (3) to give

$$\bar{\sigma}_{\text{exp}} = \frac{1}{\Phi_{\text{total}}} \left(\frac{{}^{10}\text{Be}}{{}^9\text{Be}} \right). \quad (4)$$

For this work, the ${}^{197}\text{Au}(n, \gamma){}^{198}\text{Au}$ reaction was used as the flux monitor, and initial estimates for the total neutron flux in target foils were determined by rearranging the general activation equation and solving for the flux term Φ , giving

$$\Phi = \frac{N_p(t_0)\lambda_p}{N_T \bar{\sigma} (1 - e^{-\lambda_p t_{\text{irr}}})}, \quad (5)$$

where N_T is the number of ${}^{197}\text{Au}$ target atoms, $N_p(t_0)$ is the number of ${}^{198}\text{Au}$ atoms at the end of irradiation t_0 , λ_p is the decay constant of ${}^{198}\text{Au}$, t_{irr} is the irradiation time, and $\bar{\sigma}$ is the ${}^{197}\text{Au}(n, \gamma){}^{198}\text{Au}$ reaction cross section for the given neutron spectrum. The N_T values were calculated from foil masses and the decay constant was calculated using 2.6941 ± 0.0002 d as the half-life for ${}^{198}\text{Au}$ [38]. The $\bar{\sigma}$ values for the ${}^{197}\text{Au}(n, \gamma){}^{198}\text{Au}$ reactions at each position were calculated using ENDF/B-VIII.0 data and the library preparation feature is FISPACT-II, which is based on Eq. (2), where

the energy-dependent neutron flux profiles were provided by MCNP simulations.

Since the flux estimates ultimately rely on the simulated energy neutron distributions, the simulations must be validated against experiments to assess the accuracy of the model and the systematic uncertainty of this approach. Validation efforts were conducted using the STAYSL-PNNL suite to perform neutron spectrum adjustments and the FISPACT-II code to compare activations in stainless steel. The STAYSL-PNNL suite uses a least-squares approach to adjust input neutron spectra to fit experimental reaction rates $\bar{\sigma}\phi$, correcting for irradiation history and potential self-shielding effects.

To calculate the $\bar{\sigma}\phi$ values, quantitative results from gamma assay of single element foils were first converted to saturation activities A_{sat} according to

$$A_{\text{sat}} = A(t_0)[1 - e^{-\lambda t_{\text{irr}}}]^{-1}, \quad (6)$$

where $A(t_0)$ is the activity at the end of irradiation, λ is the decay constant for a specific activation product, and t_{irr} is the irradiation time. The A_{sat} values were then normalized by foil mass and converted to $\bar{\sigma}\phi$ values according to

$$\bar{\sigma}\phi = \frac{A_{\text{sat}} W_{\text{target}}}{a_{\text{target}} N_A}, \quad (7)$$

where $A_{\text{sat}}/g_{\text{foil}}$ is the mass normalized saturation activity, W_{target} is the molecular weight of the target foil, a_{target} is the abundance of the target isotope, and N_A is Avogadro's number. The STAYSL-PNNL code then adjusts the input neutron spectrum to find a best fit to the set of experimental $\bar{\sigma}\phi$ values using a χ^2 minimization approach.

As an additional check on the validation process, the FISPACT-II code was used to perform deterministic inventory calculations for the irradiation of a stainless-steel target using the adjusted neutron spectra from the STAYSL-PNNL output. The FISPACT-II results were normalized by the mass of the stainless-steel target and compared against experimental results from gamma assay. The outputs from both the STAYSL-PNNL and FISPACT-II validation efforts were combined to assess the systematic error of the model and this approach. Finally, the adjusted total neutron fluence from the STAYSL-PNNL analysis was used with the ${}^{10}\text{Be}/{}^9\text{Be}$ ratio AMS measurements to calculate the integral cross section using Eq. (4).

III. EXPERIMENTAL METHODS

A. NCERC's Flattop foil activation experiments

The Flattop critical assembly at NCERC [20] consists of a spherical natural uranium reflector surrounding interchangeable cores, with control rods and mass buttons to enable reactivity adjustments and obtain different neutron energy profiles. The Flattop assembly also has a center transverse sample tube that spans from the far edge of the core, through the center, and out one side of the reflector. An important benefit of the Flattop assembly is that, in a given experiment, the target foil stack can be repeated at multiple locations throughout the transverse sample tube to utilize different neutron environments.

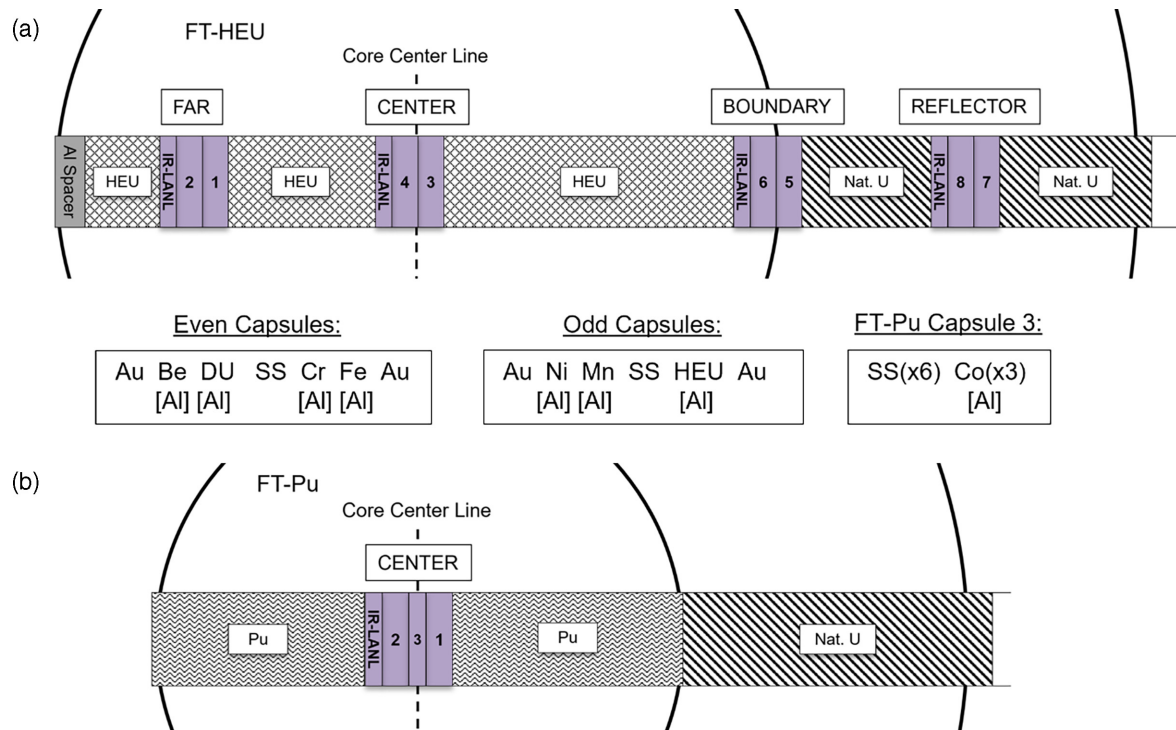


FIG. 3. Target foil pack layouts for the a) FT-HEU and b) FT-Pu experiments containing Au, Be, stainless steel (SS) and its elemental components (Cr, Mn, Fe, Ni), as well as highly enriched uranium (HEU, 93.2% ^{235}U) and depleted uranium (DU, 99.9% ^{238}U) as spectral indicators. Additional SS and Co foils were included in the FT-Pu experiment. The Ir-LANL foil was included as part of a separate ride-along experiment. Foil packs were surrounded by either HEU, natural U, or Pu plugs, depending on location, to fill the sample tube.

Two irradiation experiments were conducted: one using the highly enriched uranium (FT-HEU) core, and the other using the plutonium (FT-Pu) core. In the FT-HEU experiment, target foils were placed at four locations across the assembly as depicted in Fig 3(a). The “Far” pack is furthest into the transverse sample tube, positioned approximately halfway between the center of the core and the core/reflector boundary. The “Center” pack was placed in the middle of the HEU core. The “Boundary” pack was positioned so that the core/reflector boundary line divided the foil stack in half. The “Reflector” pack was positioned in the middle of the natural uranium reflector. The space between sample positions was filled with either HEU or natural uranium plugs, depending on the location, to keep the material consistent in the core or reflector, along with an Al spacer placed furthest inward. The irradiation lasted for 0.65 h with an integrated total charge (system power level indicator) of 0.029 A s.

The FT-Pu experiment had to be modified due to reactivity differences caused by the core swap, resulting in the exclusion of the Far, Boundary, and Reflector packs. Only the Center position foil pack was used, with an additional small capsule containing additional target foils as shown in Fig. 3(b). The modified layout resulted in reduced system power output, causing an extended run time of 5.42 h, and reduced integrated total charge of 0.0157 A s.

Thin metal target foils for both experiments included Be, Au for flux determination, stainless steel (SS) and its major component elements (Cr, Mn, Fe, Ni) for neutron spectrum analysis and validation, as well as HEU and depleted uranium

(DU) as additional spectral indicators (additional details provided in Ref. [21]). The metal foil targets (excluding Be, HEU, and DU) were from Shieldwrx or Goodfellow and 99.8% purity or better. The HEU and DU foils were characterized to obtain U isotopics, while the Be foils were checked for B contamination since the $^{10}\text{B}(n, p)^{10}\text{Be}$ reaction cross section is at least two orders of magnitude larger at the neutron energies in this work [11,15]. The Be foil masses and intrinsic $^{10}\text{Be}/^9\text{Be}$ atom ratios of the target materials are shown in Table I. All other single element foils had natural isotopic composition, while the SS foils were type 304, the HEU was 93.2% ^{235}U , and the DU was 99.9% ^{238}U (Ir foils were included as separate ride-along experiment that is beyond the scope of this work). Target foils were packaged in Al capsules, with some foils being wrapped in additional Al foils (see Fig. 3) for safety and contamination considerations, and to limit crosstalk during the irradiation. The added capsule for the FT-Pu experiment included Co as another spectrum constraint and additional SS foils.

B. Activation product measurements

Activation products in irradiated foils were measured through gamma spectrometry, except for the Be foils which were assayed via AMS. Irradiated foils were separated and dissolved individually, including Al wraps when present, in Aqua Regia, nitric acid, or hydrochloric acid, as required. Solutions were reduced to a minimum volume through evaporative heating, transferred to a gamma counting vial, and

TABLE I. Intrinsic ${}^{10}\text{Be}/{}^9\text{Be}$ ratios and metal foil masses.

Experiment	Intrinsic ${}^{10}\text{Be}/{}^9\text{Be}$ Ratio (10^{-14} at/at)	Position	Foil mass (mg)
FT-HEU	0.74 ± 0.04	Far	20.7 ± 0.3
		Center	20.0 ± 0.3
		Boundary	20.8 ± 0.3
		Reflector	20.2 ± 0.3
FT-Pu	1.65 ± 0.08	Center	20.0 ± 0.3

diluted to a final volume before analysis. Gamma spectrometry was performed on each sample, with a minimum of three measurements made per sample across different detectors. The detectors were ORTEC p-type high-purity germanium detectors with relative efficiencies of 12–37%. Data acquisition was performed using ORTEC DSPEC units, using 4096 channels up to 2 MeV. Counting distances were optimized to reduce summing and count times while achieving better than 3% uncertainty in the counting statistics of the primary gamma peaks. The resulting gamma spectra were analyzed by the GAMANAL [39] program to account for efficiencies, calculate peak areas, and resolve interfering peaks. The GAMANAL outputs were processed by an in-house data reduction tool following the Multi-Agency Radiological Laboratory Analytical Protocols Manual [40] standards to calculate final weighted averages of atoms per sample, corrected for decay during counting and decay corrected to the end of irradiation.

The Be foils and their Al wraps were dissolved together in hydrochloric acid because of difficulties in separating the foils from the wraps, and also to prepare the Al component for gamma analysis. Due to *in situ* cosmogenic production of ${}^{10}\text{Be}$, there is a nontrivial background in Be and Al sources. Because of this, a series of unirradiated Be and Al foils were measured as material blanks to correct for the natural ${}^{10}\text{Be}$ background (see Table I for ${}^{10}\text{Be}/{}^9\text{Be}$ ratios in the Be foil blanks). Unirradiated Al material blanks required the addition of low-level Be carrier (Purdue Rare Isotope Measurement Laboratory, West Lafayette, IN, USA) to ensure Be levels above detection limits for analysis and determine any background contributions from Al foils. No purification steps were performed, and samples were precipitated with aqueous ammonia at $\text{pH} = 8$. The precipitated hydroxides were rinsed and redissolved in nitric acid before being transferred to quartz crucibles and calcined at 800°C for 30 minutes in a muffle furnace. The resulting oxides were mechanically mixed with high-purity Nb powder (Puratronic, Alfa-Aesar, USA) in a 1:1 ratio by mass. Mixtures were loaded into individual samples holders for AMS and measured in duplicate using established procedures [41]. The AMS results were normalized to the ICN 01-5-4 standard, using the revised ${}^{10}\text{Be}/{}^9\text{Be}$ ratio value of $(2.851 \pm 0.031) \times 10^{-12}$ at/at from Nishiizumi *et al.* [42].

IV. SIMULATION AND VALIDATION

A. Flattop simulation with MCNP

The experimental conditions were simulated in MCNP6.3 using a high-fidelity model of the Flattop critical assembly

with either the HEU or Pu core. The foil packs were modeled using a lattice construction within the dimensions of each capsule, with the number of voxels equal to the number of foils in each capsule. Target foils were based on the SS foil geometry, having a radius of 4 mm and thickness of 0.02 mm. The Al foil wraps assumed a uniform thickness of 0.02 mm on all sides. A series of F4 tallies with 1000 logarithmically spaced energy bins were used in each of the Au foils to estimate the neutron flux and energy distributions. Extended runs of the simulations using current ENDF/B-VIII.0 nuclear data were performed using high-performance computing resources at Lawrence Livermore National Laboratory to improve tally statistics.

The tally results in each of the Au foils were converted to probability distributions for use in Eq. (2) to calculate 1-group cross sections and estimate the neutron flux seen by each Au foil using Eq. (5). Since the overall lengths of the foil packs were small (0.635 cm), the neutron distributions were not expected to change significantly within an individual location. Therefore, the four Au tallies at each location were averaged together to provide a single neutron distribution representative of the foil pack location for use in the validation efforts. The individual neutron tallies were characterized by the average neutron energy of the combined distributions.

B. Neutron spectrum adjustment and validation

The first step in validating the simulation was to perform neutron spectrum adjustments using the STAYSL-PNNL suite [23]. Quantitative results for selected activation products from gamma assay of single element foils were used as constraints for the adjustment process. The selected activation products were chosen based on the availability of single pathway production channels and whether the reactions were present in the International Reactor Dosimetry and Fusion File version 1.05 [43], a library created specifically for neutron metrology applications. The experimental $\bar{\sigma}\phi$ values for the reactions listed in Table II were calculated using the tools within the STAYSL-PNNL suite, following Eqs. (6) and (7). Weighted averages of the activation products in the Au foils were calculated for each position, based on the assumption of minimal change to the neutron spectrum with the distance of the foil pack.

The position-averaged neutron spectrum at each location was used as the initial guess spectrum in the adjustment process. Analysis with STAYSL-PNNL was performed using a 725-group structure and an expanded uncertainty treatment. An energy-dependent block uncertainty scheme for the simulated neutron distributions was estimated for the STAYSL analysis. The block uncertainties were 30% for 10 eV to

TABLE II. Single pathway neutron induced reactions available as constraints in the neutron spectrum adjustment process.

Element	Target	Ejectile	Residual	Threshold ^a (MeV)
Mn	⁵⁵ Mn	2n	⁵⁴ Mn	10.4139 ± 0.0011
Fe	⁵⁴ Fe	p	⁵⁴ Mn	Yes
	⁵⁴ Fe	α	⁵¹ Cr	Yes
	⁵⁸ Fe	γ	⁵⁹ Fe	No
Ni	⁵⁸ Ni	2n	⁵⁷ Ni	12.4290 ± 0.0005
	⁵⁸ Ni	p	⁵⁸ Co	Yes
	⁶⁰ Ni	p	⁶⁰ Co	2.0748 ± 0.0006
Co	⁵⁹ Co	γ	⁶⁰ Co	No
	⁵⁹ Co	p	⁵⁹ Fe	0.7959 ± 0.0005
Au	¹⁹⁷ Au	2n	¹⁹⁶ Au	8.114 ± 0.003
	¹⁹⁷ Au	γ	¹⁹⁸ Au	No

^aThreshold reactions defined by STAYSL-PNNL [24] (indicated by “Yes” or numeric values) have cross sections of 0.0 b at 10⁻¹⁰ MeV; numeric values are from the National Nuclear Data Center QCalc tool [44].

1 keV, 10% from 1 keV to 1 MeV, 5% for 1–8 MeV, and 20% for 8–20 MeV. The STAYSL-PNNL adjustment process was iterated to optimize the normalized- χ^2 metric, an assessment of the quality of results (value of 1 indicating a good result), by removing reactions that heavily skewed the normalized- χ^2 value while still including as many reactions as possible. The average deviation between experimental and adjusted $\bar{\sigma}\phi$ values for each location was used to estimate the systematic error of the simulation and method.

The second component of the validation approach was to use the FISPACT-II code [24] to perform activation calculations for an SS target using the adjusted neutron spectra from the STAYSL-PNNL analysis. The adjusted neutron spectra were converted to the 709-group structure in FISPACT-II and used ENDF/B-VIII.0 reaction cross-section data. An arbitrary thin foil SS target was used, and the results were normalized by foil mass to give atoms per gram at the end of irradiation. The results from the FISPACT-II calculations were compared against experimental results from gamma assay of the SS foils. Again, the average deviations between calculation and experiment were used to assess the systematic uncertainty at each location. The final systematic uncertainty component was determined by averaging both the STAYSL-PNNL and FISPACT-II assessments for each location.

V. RESULTS AND DISCUSSION

A. Simulated neutron spectra and flux estimates

The individual tally spectra in each of the Au foils for a given location were statistically similar in both experiments, showing only minor deviations at the highest and lowest neutron energies. Only the Boundary position in the FT-HEU experiment, shown in Fig. 4, displayed any significant change within the dimensions of the foil pack. Since the Boundary position for the FT-HEU covers the transition from HEU to natural U in the Flattop assembly, the neutron spectrum is expected to change and shift to lower neutron energies. This evolution of the neutron spectrum can be seen in Fig. 4 by moving from Capsule-6 Left (most inward, HEU side) to Capsule-5 Right (most outward, natural U side).

The simulated energy distributions were combined with ENDF/B-VIII.0 cross-section data to calculate $\bar{\sigma}$ values according to Eq. (2), using the library preparation feature of the FISPACT-II code. From there, the total flux values were calculated for each Au foil using Eq. (5) and the gamma spectrometry results from the ¹⁹⁸Au analysis. To better compare the two experiments and account for different power levels and irradiation times, the total neutron fluence and average simulated neutron energies are plotted in Fig. 5. The total fluence [Fig. 5(a)] and average neutron energy values [Fig. 5(b)] are consistent within a given foil pack location for both experiments, except for the FT-HEU Boundary pack which shows the greatest variation. Both the total fluence and average neutron energy values show similar trends in the FT-HEU experiment, peaking at the center of the assembly, falling off as distance from center increases, and then leveling out in the natural U reflector.

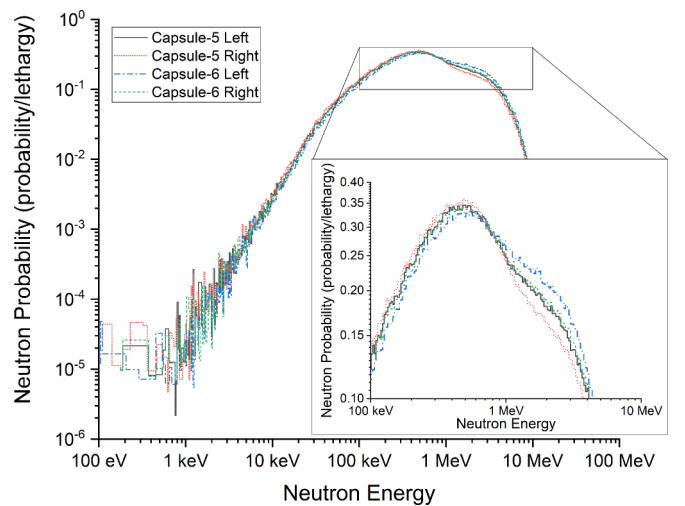


FIG. 4. Simulated neutron spectra at the Boundary position in the FT-HEU simulation for the four Au foils covering the transition from HEU to natural U in the Flattop assembly, with Capsule-6 Left (dash-dot, blue) being the most inward on the HEU side and Capsule-5 Right (short dot, red) being the most outward on the natural U side. Individual bin uncertainties omitted for clarity.

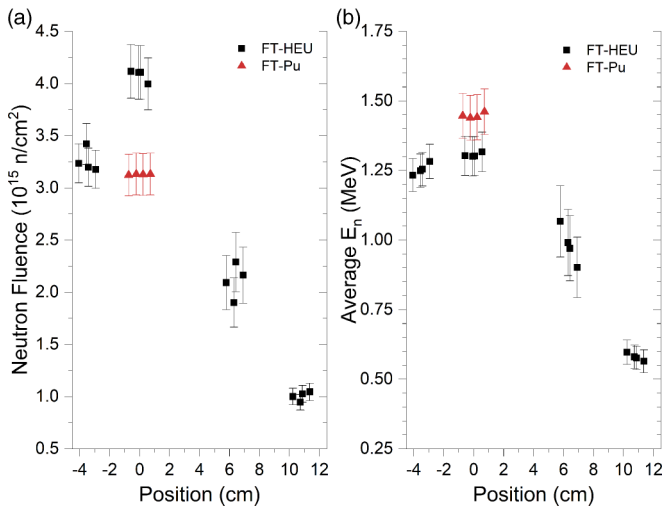


FIG. 5. Total neutron fluence (a) and average neutron energy (b) in Au foils for the FT-HEU (square, black) and FT-Pu (triangle, red) experiments as a function of distance from the center of the assembly. Error bars are 1σ combined uncertainty (see Sec. V C, Table IV for systematic component).

The individual neutron spectra at each position were combined to generate the position-averaged neutron distributions shown in Fig. 6, where the softening of the neutron spectrum outwards from the center of the core is easier to see on the coarser distance scale. The Far and Center positions in the FT-HEU experiment are very similar, with the Far distribution showing slightly higher probabilities at lower neutron energies. The Center position for the FT-Pu experiment is similar to that of the FT-HEU Center position, peaking at slightly higher energy values. The FT-HEU Boundary distribution shows a significant departure from the Far and Center distributions, having a more discernable peak near 500 keV and higher probabilities favoring lower neutron energies at

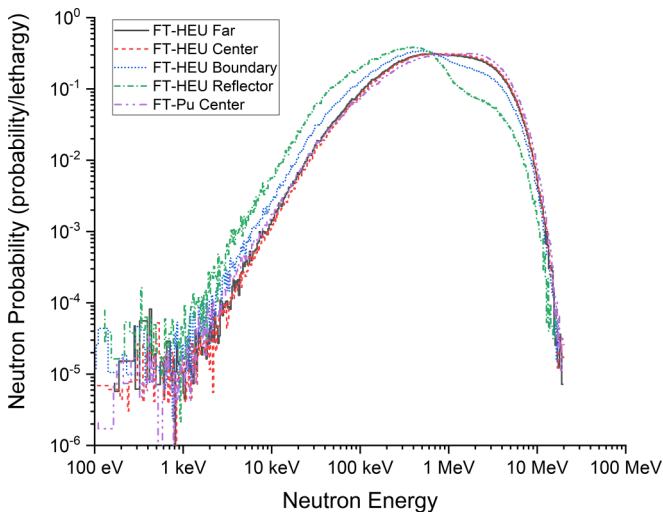


FIG. 6. Simulated position-averaged neutron energy distributions for the foil pack locations in the FT-HEU and FT-Pu experiments. Bin uncertainties omitted for clarity.

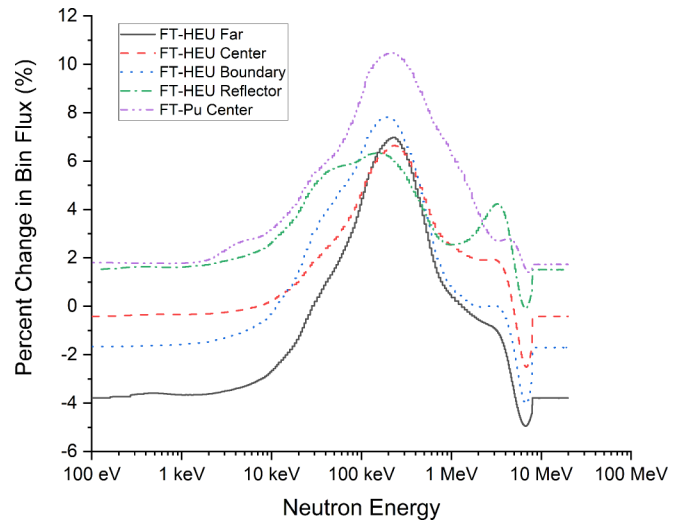


FIG. 7. The relative difference between the STAYSL-PNNL adjusted neutron spectra and the MCNP input spectra is shown for each location within the assembly.

the expense of high energy neutrons. The softening trend continues in the Reflector distribution where the shift to lower neutron energies is even more pronounced.

B. Adjusted neutron spectra

The position-averaged neutron distributions were combined with experimental $\bar{\sigma}\phi$ values as input for the STAYSL-PNNL adjustment. Figure 7 shows the bin-wise relative adjustments made for the average neutron distribution at each position, the result being that most adjustments have a magnitude less than 10%. All positions show a similar trend of adjustments, differing slightly in magnitude.

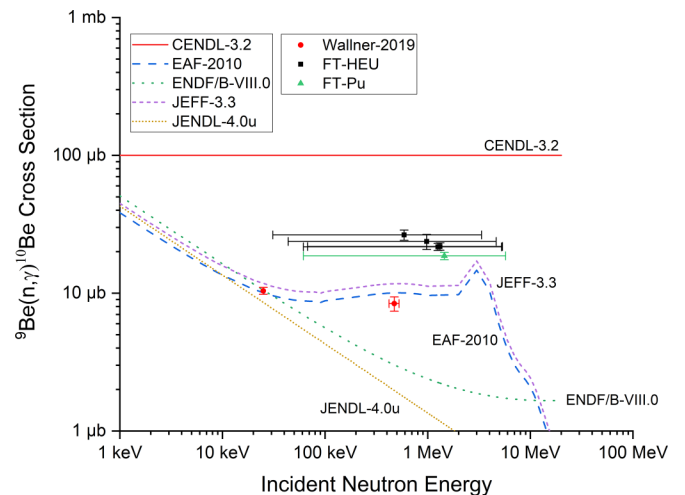


FIG. 8. Plot of the integral cross sections from this work (FT-HEU: square, black; FT-Pu: triangle, green) along with the current nuclear data libraries and only other existing data (red, circle) in this energy range. The X-axis error bars for this work represent 95% of the neutron energy distributions.

TABLE III. Neutron spectrum metrics before and after the STAYSL-PNNL adjustment process with 1σ statistical uncertainties.

Experiment	Position	\bar{E}_n (MeV)			Total flux (10^{11} n/cm ² s)		
		Simulated	Adjusted	% increase	Simulated	Adjusted	% increase
FT-HEU	Far	1.254 ± 0.006	1.26 ± 0.09	6.8	13.90 ± 0.28	14.2 ± 0.4	2.0
	Center	1.304 ± 0.010	1.32 ± 0.09	6.8	17.40 ± 0.17	18.0 ± 0.5	3.4
	Boundary	0.9716 ± 0.0029	0.98 ± 0.08	7.8	8.9 ± 0.4	9.19 ± 0.29	3.5
	Reflector	0.529 ± 0.007	0.59 ± 0.05	8.7	4.28 ± 0.09	4.48 ± 0.14	4.7
FT-Pu	Center	1.446 ± 0.007	1.46 ± 0.11	7.4	1.57 ± 0.02	1.67 ± 0.05	6.4

The effects of the adjustment on the neutron spectra are shown in Table III, including before and after values for average neutron energy and total neutron flux, along with the relative differences. For all positions, there is a slight increase in average neutron energy from the adjustment process and significantly more uncertainty. The effect of the adjustment process on the final flux values is minimal.

C. Validation, assessment, and uncertainty

To validate the models and build confidence in the neutron spectra, outputs from both the STAYSL-PNNL adjustment and FISPACT-II inventory calculation were compared against experimental results and are presented in Table IV. For the STAYSL-PNNL validation, adjusted $\bar{\sigma}\phi$ values calculated using the adjusted neutron spectra were compared against the experimental $\bar{\sigma}\phi$ values for the reactions listed in Table I. Not all nine reactions were used for each position, due to optimizing the normalized- χ^2 parameter (good fit = 1). The normalized- χ^2 values for the Far and both Center locations indicate good fits to the experimental reaction rates. The fits for the Boundary and Reflector positions in the FT-HEU experiments are not as good, as indicated by normalized- χ^2 values further from unity. The standard deviation for the STAYSL-PNNL analysis is presented as the average of the magnitude of relative deviations between the adjusted and experimental $\bar{\sigma}\phi$ values for the set of reactions used for each location and range from 3.5% at the FT-HEU Reflector position to 14.5% at the FT-HEU Boundary.

The FISPACT-II inventory calculation assessment was slightly different in that atoms per gram values of activation products normalized to the SS target mass were determined for a simulated irradiation of SS using the adjusted neutron spectra and adjusted flux values from the STAYSL-PNNL analysis. In this assessment, all production pathways in

ENDF/B-VIII.0 data are considered for a given activation product. The number of activation products referenced in Table IV includes analysis of all SS targets at each position (see Fig. 3) and is not reflective of the number of unique activation products. The activation products considered were ⁵¹Cr, ⁵⁴Mn, ^{57,58}Co, and ⁵⁷Ni. The standard deviation for the FISPACT-II assessment is the average magnitude of the relative deviations between calculated and experimental atoms per gram values. The standard deviations range from 4.8% for the FT-HEU Far position to 12.0% at the FT-HEU Boundary position.

The results from both validation assessments were averaged together for each position to give results that correlate well with position from the center of the assembly: 4.8% for FT-HEU Far, 5.4% for FT-HEU Center, 12.0% for FT-HEU Boundary, 7.3% for FT-HEU Reflector, and 5.6% for FT-Pu Center. These combined values were used as an estimate of the systematic uncertainty of the MCNP models and the approach used in this work.

The major contributors to the overall uncertainty are detailed in Table V. The uncertainty budget can be divided into three categories, simulation, experimental, and data analysis, with each category having both statistical and systematic uncertainty components. For the simulation category, the main contributor is the systematic uncertainty of the model, while the statistical component was minimized using high-performance computing resources. In the experimental category, the primary sources of uncertainty originated from measurement operations. Gamma spectrometry measurements were conducted to achieve the best possible counting statistics in a reasonable timeframe and also included a 3% systematic component from the detector calibration. The overall error in the activation product measurements was able to be kept low through replicate analysis and weighted averages. The uncertainty from the AMS measurements was in the

TABLE IV. Validation assessment for STAYSL-PNNL and FISPACT-II analyses.

Experiment	Position	STAYSL adjustment			FISPACT-II activation		
		Number of reactions	Normalized χ^2	% standard Deviation	Number of activation Products	% Standard Deviation	Average % standard Deviation
FT-HEU	Far	6	1.074	5.3	8	4.3	4.8
	Center	5	1.201	5.3	8	5.5	5.4
	Boundary	4	2.411	14.5	8	9.5	12.0
	Reflector	7	0.753	3.5	8	11.1	7.3
FT-Pu	Center	6	1.055	3.8	15	7.4	5.6

TABLE V. Uncertainty budget contributions of statistical and systematic components.

Uncertainty Source	Category/Type	Estimated value (%)
MCNP tally output	Simulation/statistical	2
Model implementation	Simulation/systematic	12
${}^{198}\text{Au}$ gamma counting	Experimental/statistical	1
Gamma detector calibration	Experimental/systematic	3
AMS measurements	Experimental/statistical	5
AMS ${}^{10}\text{Be}/{}^9\text{Be}$ standard	Experimental/systematic	1.1
Foil masses	Experimental/systematic	2
Time keeping	Analysis/systematic	1
${}^{198}\text{Au}$ nuclear data	Analysis/systematic	1
Total upper estimate		14

range of 2–5%, while the systematic uncertainty associated with the ICN 01-5-4 standard was 1.1% [42]. Uncertainty due to foil masses was determined to be negligible relative to other uncertainty components. The final category of uncertainty drivers is data analysis, which focuses on nuclear data and mathematical operations. Uncertainties related to time factors during data reduction were also found to be negligible in the overall uncertainty budget. Cross section and decay data uncertainties varied based on nuclide but were only relevant for ${}^{198}\text{Au}$ in this analysis since it was used for flux determination. The uncertainties regarding other decay data for other activation products contributed to the final uncertainties for nuclides used as constraints in the validation process and are indirectly represented by the systematic uncertainty of the model.

D. ${}^{10}\text{Be}/{}^9\text{Be}$ measurements and integral cross sections

The ${}^{10}\text{Be}/{}^9\text{Be}$ ratio in each Be foil as measured by AMS is shown in Table VI, along with the blank-corrected values and the weighted mean of the duplicate measurements. The measured values were corrected for Be (see Table I) and Al material blanks as well as reagent blanks. The experimental ${}^9\text{Be}(n, \gamma){}^{10}\text{Be}$ integral cross-section values were calculated from the corrected averages using Eq. (4) and the adjusted

neutron fluence values from the STAYSL-PNNL analysis and are also presented in Table VI.

The experimental integral cross sections are plotted with the nuclear data libraries and the Wallner *et al.* [5] data in Fig. 8 (horizontal error bars for this work represent 95% of the neutron energy distribution). The values from this work are $26.5 \pm 2.2 \mu\text{b}$ at 0.59 ± 0.07 MeV, $24 \pm 3 \mu\text{b}$ at 0.98 ± 0.14 MeV, $21.7 \pm 1.3 \mu\text{b}$ at 1.26 ± 0.11 MeV, $21.8 \pm 1.4 \mu\text{b}$ at 1.32 ± 0.11 MeV, and $18.6 \pm 1.1 \mu\text{b}$ at 1.46 ± 0.13 MeV. These values do not align with the current nuclear data libraries and are two to three times greater than the data point at a nearby energy.

To further evaluate the results from this work, integral cross sections were calculated for the major nuclear data libraries using the adjusted neutron spectra and are presented in Table VII. The calculated library integral cross sections range from 1.8 to $100 \mu\text{b}$, depending on the position-library combination, and none agree with values from this work (library uncertainties are 16–28%, when available). The JEFF-3.3/BROND-3.1 libraries are closest due to their additional consideration of higher energy resonances. A poorly characterized thermal component of the neutron energy distributions, which would increase the calculated integral cross sections, is unlikely given the accuracy of the validation results, particularly regarding nonthreshold reactions. Additional analysis

TABLE VI. Measured, corrected, and average values for the ${}^{10}\text{Be}/{}^9\text{Be}$ ratio measured by accelerator mass spectrometry and associated experimental cross sections with 1σ combined uncertainties.

Experiment	Sample	${}^{10}\text{Be}/{}^9\text{Be}$ ratio (10^{-14} at/at)			$\bar{\sigma}_{\text{exp}}$ (μb)
		Measured	Corrected	Weighted mean	
FT-HEU	Far-A	7.93 ± 0.20	7.12 ± 0.29	7.19 ± 0.23	21.7 ± 1.3
	Far-B	8.1 ± 0.3	7.3 ± 0.4		
	Center-A	9.88 ± 0.27	9.1 ± 0.4	9.21 ± 0.26	21.8 ± 1.4
	Center-B	10.10 ± 0.21	9.3 ± 0.3		
	Boundary-A	5.74 ± 0.19	4.94 ± 0.24	5.10 ± 0.17	24 ± 3
	Boundary-B	6.06 ± 0.17	5.25 ± 0.24		
	Reflector-A	3.53 ± 0.13	2.73 ± 0.16	2.78 ± 0.12	26.5 ± 2.2
	Reflector-B	3.61 ± 0.13	2.82 ± 0.16		
FT-Pu	Center-A	7.70 ± 0.14	6.04 ± 0.16	6.06 ± 0.12	18.6 ± 1.1
	Center-B	7.74 ± 0.16	6.09 ± 0.18		

TABLE VII. Experimental integral cross sections in the MeV neutron energy range compared against evaluated nuclear data libraries.

	\bar{E}_n (MeV)	$\bar{\sigma}_{\text{exp}}$ (μb)	Evaluated integral cross sections (μb)				
			CENDL-3.2	EAF-2010	ENDF/B-VIII.0; TENDL-2019	JEFF-3.3; BROND-3.1	JENDL-4
FT-HEU	1.26 ± 0.11	21.7 ± 1.3	100	9.8	3.1	11.5	2
	1.32 ± 0.11	21.8 ± 1.4	100	9.9	3	11.5	1.9
	0.98 ± 0.14	24 ± 3	100	9.8	3.4	11.4	2.3
	0.59 ± 0.07	26.5 ± 2.2	100	9.6	4.1	11.2	2.9
FT-Pu	1.46 ± 0.13	18.6 ± 1.1	100	9.8	2.9	11.5	1.8
Wallner-2019 ^a	0.025^b	10.4 ± 0.6		–	9.7	11.8	7.9
	0.473 ± 0.053	8.4 ± 1.0		–	3.1	11.6	2

^aData from [5].

^bQuasi-Maxwellian spectrum at $kT = 25$ keV with no reported uncertainty.

of Be stock material also excluded any possible B contamination that could artificially inflate the ^{10}Be value from the $^{10}\text{B}(n, p)^{10}\text{Be}$ reaction. Therefore, the discrepancies presented in this work suggest a more complex cross section in the MeV energy range for the $^9\text{Be}(n, \gamma)^{10}\text{Be}$ reaction, particularly regarding the 622 and 811 keV resonances as suggested by Wallner [5] and Mohr [18], as well as the unresolved resonances listed by Mughabghab [19] at 2.710 and 2.850 MeV.

VI. SUMMARY

This work coupled simulation and experiment to investigate the $^9\text{Be}(n, \gamma)^{10}\text{Be}$ integral cross section in an unstudied energy regime. Foil activation experiments were performed using the Flattop critical assembly at the National Criticality Experiments Research Center as the neutron source, investigating activations by neutron spectra created with both the HEU and Pu cores. The $^{10}\text{Be}/^9\text{Be}$ ratio was measured through accelerator mass spectrometry and the experiment was simulated using MCNP to determine the total neutron fluence. Simulated neutron spectra were validated against experimental activation product results using the STAYSL-PNNL suite and the FISFACT-II code. The new integral cross sections from this work range from $26.5 \pm 2.2 \mu\text{b}$ at 0.59 ± 0.07 MeV to $18.6 \pm 1.1 \mu\text{b}$ at 1.46 ± 0.13 MeV, and do not align with existing data or the nuclear data library evaluations. The

discrepancies reported here point to a more complex cross-section structure in the MeV energy range that should include additional resonance considerations that are not represented by the current evaluations. More work is necessary to further constrain cross-section library evaluations and determine the true shape of the $^9\text{Be}(n, \gamma)^{10}\text{Be}$ cross section at non-thermal neutron energies.

ACKNOWLEDGMENTS

This work was performed under the auspices of the U.S. Department of Energy by Lawrence Livermore National Laboratory under Contract No. DE-AC52-07NA27344.LLNL-JRNL-853075. This work was funded by the Office of Defense Nuclear Nonproliferation Research and Development within the U.S. Department of Energy's National Nuclear Security Administration. The authors would like to acknowledge the contributions of Todd Bredeweg and David Hayes at Los Alamos National Laboratory for facilitating the experiments at NCERC, as well as Keenan Thomas and Todd Woody of the Nuclear Counting Facility at Lawrence Livermore National Laboratory for conducting the gamma assay measurements. The authors also thank Boris Pritychenko at Brookhaven National Laboratory for providing essential references, Jason Harke at Lawrence Livermore National Laboratory for discussions regarding resonance considerations, and Alan Hidy at Lawrence Livermore National Laboratory for Be AMS measurement expertise.

- [1] M. Wróblewska, D. Blanchet, A. Lyoussi, P. Blaise, J. Jagielski, Z. Marcinkowska, A. Boettcher, T. Machtyl, M. Jauchta, and I. Wilczek, *Ann. Nucl. Energy* **163**, 108540 (2021).
- [2] J. Görres, H. Herndl, I. J. Thompson, and M. Wiescher, *Phys. Rev. C* **52**, 2231 (1995).
- [3] A. Bartlett, J. Görres, G. J. Mathews, K. Otsuki, M. Wiescher, D. Frekers, A. Mengoni, and J. Tostevin, *Phys. Rev. C* **74**, 015802 (2006).
- [4] K. Farouqi, K.-L. Kratz, B. Pfeiffer, T. Rauscher, F.-K. Thielemann, and J. W. Truran, *Astrophys. J.* **712**, 1359 (2010).
- [5] A. Wallner, M. Bichler, L. Coquard, I. Dillmann, O. Forstner, R. Golser *et al.*, *Phys. Rev. C* **99**, 015804 (2019).
- [6] R. B. Firestone and Z. Revay, *Phys. Rev. C* **93**, 054306 (2016).
- [7] C. M. Conneely, W. V. Prestwich, and T. J. Kennett, *Nucl. Instrum. Methods Phys. Res., Sect. A* **248**, 416 (1986).
- [8] H. Rose, W. A. Cooper, and R. B. Tattersall, in *Physics and Mathematics. Series I. Progress in Nuclear Energy* (Pergamon, London, 1959), Vol. 3, p. 292.
- [9] W. Palevsky, 1952, EXFOR 11204.002.
- [10] K. Shibata *et al.*, *J. Nucl. Sci. Technol.* **48**, 1 (2011).
- [11] D. A. Brown *et al.*, *Nucl. Data Sheets* **148**, 1 (2018).

- [12] J. Koning, D. Rochman, J. Sublet, N. Dzysiuk, M. Fleming, and S. van der Marck, *Nucl. Data Sheets* **155**, 1 (2019).
- [13] Z. Ge *et al.*, *EPJ Web Conf.* **239**, 09001 (2020).
- [14] A. I. Blokhin, E. V. Gai, A. V. Ignatyuk, I. I. Koba, V. N. Manokhin, and V. N. Pronyaev, *Probl. At. Sci. Technol. Ser. Nucl. Reactor* **2**, 62 (2016).
- [15] A. J. M. Plompen *et al.*, *Eur. Phys. J. A* **56**, 181 (2020).
- [16] J.-Ch. Sublet, L. W. Parker, J. Kopecky, R. A. Forrest, A. J. Koning, and D. A. Rochman, Technical Report CCFE-R(10)05, Culham Center for Fusion Energy, UK Atomic Energy Authority, 2010 (unpublished).
- [17] R. A. Forrest and J. Kopecky, UK Atomic Energy Authority Technical Report No. UKAEA FUS 451, 2001 (unpublished).
- [18] P. Mohr, *Phys. Rev. C* **99**, 055807 (2019).
- [19] S. F. Mughabghab, in *Atlas of Neutron Resonances*, 6th ed. (Elsevier, Amsterdam, 2018), Recommended Thermal Cross Sections, Resonances Properties, and Resonance parameters for $Z = 1-60$, p. 103.
- [20] D. Hayes *et al.*, *Nucl. Sci. Eng.* **195**, S37 (2021).
- [21] J. A. Church, B. B. Bandong, J. J. Goodell, N. K. Harward, C. Keith, S. W. Padgett, K. E. Roberts, and P. Zhao, *J. Radioanal. Nucl. Chem.* **332**, 2167 (2023).
- [22] M. E. Rising *et al.*, Los Alamos National Laboratory Technical Report LA-UR-22-33103, Rev. 1, 2023.
- [23] L. R. Greenwood and C. D. Johnson, Pacific Northwest National Laboratory Technical Report No. PNNL-22253, 2013 (unpublished).
- [24] J.-Ch. Sublet, J. W. Eastwood, J. G. Morgan, M. R. Gilbert, M. Fleming, and W. Arter, *Nucl. Data Sheets* **139**, 77 (2017).
- [25] J. Chmeleff, F. von Blanckenburg, K. Kossert, and D. Jakob, *Nucl. Instrum. Methods Phys. Res., Sect. B* **268**, 192 (2010).
- [26] G. Korschinek *et al.*, *Nucl. Instrum. Methods Phys. Res., Sect. B* **268**, 187 (2010).
- [27] J. C. Davis *et al.*, *Nucl. Instrum. Methods Phys. Res., Sect. B* **52**, 269 (1990).
- [28] A. Wallner *et al.*, *Phys Rev C* **93**, 045803 (2016).
- [29] D. Baliu-Rodriguez, B. J. Stewart, and T. J. Ognibene, *J. Chromatogr. B* **1216**, 123590 (2023).
- [30] T. L. Bailey, A. M. Clark, L. Callahan, A. D. Nelson, M. Paul, M. Schiffer, D. Blankenstein, and P. Collon, *Nucl. Instrum. Methods Phys. Res., Sect. B* **536**, 1 (2023).
- [31] X. Wang *et al.*, *Nucl. Instrum. Methods Phys. Res., Sect. B* **361**, 34 (2015).
- [32] S. Pavetich *et al.*, *Nucl. Instrum. Methods Phys. Res., Sect. B* **527**, 45 (2022).
- [33] D. Pacesila, I. Stanciu, C. Simion, S. Galin, M. Mirea, M. Lechintan, P. Mereuta, and V. Mosu, *Nucl. Instrum. Methods Phys. Res., Sect. B* **539**, 43 (2023).
- [34] L. Zheng, H. Matsuzaki, and T. Yamagata, *Nucl. Eng. Technol.* **54**, 4636 (2022).
- [35] E. Chamizo, M. López-Lora, and M. Christl, *Nucl. Instrum. Methods Phys. Res., Sect. B* **533**, 81 (2022).
- [36] A. Wallner, L. K. Fifield, M. B. Froehlich, D. Koll, G. Leckenby, M. Martschini, S. Pavetich, S. G. Time, D. Schumann, and Z. Slavkoscá, *Nucl. Instrum. Methods Phys. Res., Sect. B* **534**, 48 (2023).
- [37] E. Chávez *et al.*, *Nucl. Instrum. Methods Phys. Res., Sect. B* **526**, 77 (2022).
- [38] H. Xiaolong and K. Mengxiao, *Nucl. Data Sheets* **133**, 221 (2016).
- [39] R. Gunnink and J. Niday, University of California Radiation Laboratory Technical Report No. UCRL-51061, Vols. 1-3 (unpublished).
- [40] Multi-Agency Radiological Laboratory Analytical Protocols Manual, U.S. Nuclear Regulatory Commission Report NUREG-1576, 2004, Vol. II, Chap. 16.
- [41] D. H. Rood, S. Hall, T. P. Guilderson, R. C. Finkel, and T. A. Brown, *Nucl. Instrum. Methods Phys. Res., Sect. B* **268**, 730 (2010).
- [42] K. Nishiizumi, M. Imamura, M. W. Caffee, J. R. Southon, R. C. Finkel, and J. McAninch, *Nucl. Instrum. Methods Phys. Res., Sect. B* **258**, 403 (2007).
- [43] E. M. Zsolnay, R. Capote, H. K. Nolthenius, and A. Trkov, IAEA Technical Report No. INDC(NDS)-0616, 2012 (unpublished).
- [44] T. W. Burrow, QCalc Q-Value Calculator, National Nuclear Data Center, Brookhaven National Laboratory, 2023.